

Polaron-electron assisted giant dielectric dispersion in SrZrO₃ high-k dielectric

Hitesh Borkar, Arun Barvat, Prabir Pal, A. K. Shukla, J. J. Pulikkotil, and Ashok Kumar

Citation: *Journal of Applied Physics* **119**, 214101 (2016); doi: 10.1063/1.4952710

View online: <http://dx.doi.org/10.1063/1.4952710>

View Table of Contents: <http://scitation.aip.org/content/aip/journal/jap/119/21?ver=pdfcov>

Published by the [AIP Publishing](#)

Articles you may be interested in

[Origin of giant permittivity and high-temperature dielectric anomaly behavior in Na_{0.5}Y_{0.5}Cu₃Ti₄O₁₂ ceramics](#)

J. Appl. Phys. **113**, 224102 (2013); 10.1063/1.4809927

[Dynamics of crystallization and phase transition in La_{0.5}Sr_{0.5}CoO₃ thin films](#)

Appl. Phys. Lett. **80**, 4333 (2002); 10.1063/1.1482417

[Dielectric loss anomaly and polaron hopping conduction of Gd_{1/3}Sr_{2/3}FeO₃](#)

J. Appl. Phys. **90**, 2455 (2001); 10.1063/1.1388600

[Electronic transport by small polarons in La_{0.5}Sr_{0.5}MnO₃](#)

J. Appl. Phys. **90**, 1891 (2001); 10.1063/1.1385356

[Magnetic, dielectric, and transport properties of La_{1-x}Sr_xMnO₃ at submillimeter wavelengths](#)

J. Appl. Phys. **83**, 7180 (1998); 10.1063/1.367675

The new SR865 2 MHz Lock-In Amplifier ... \$7950



SRS Stanford Research Systems
www.thinkSRS.com · Tel: (408)744-9040



Chart recording



FFT displays



Trend analysis

Features

- Intuitive front-panel operation
- Touchscreen data display
- Save data & screen shots to USB flash drive
- Embedded web server and iOS app
- Synch multiple SR865s via 10 MHz timebase I/O
- View results on a TV or monitor (HDMI output)

Specs

- 1 mHz to 2 MHz
- 2.5 nV/√Hz input noise
- 1 μs to 30 ks time constants
- 1.25 MHz data streaming rate
- Sine out with DC offset
- GPIB, RS-232, Ethernet & USB

Polaron-electron assisted giant dielectric dispersion in SrZrO₃ high-k dielectric

Hitesh Borkar,^{1,2} Arun Barvat,^{1,2} Prabir Pal,^{1,2} A. K. Shukla,¹ J. J. Pulikkotil,^{1,2,3} and Ashok Kumar^{1,2,a)}

¹CSIR-National Physical Laboratory, Dr. K. S. Krishnan Marg, New Delhi 110012, India

²Academy of Scientific and Innovative Research (AcSIR), CSIR-National Physical Laboratory (CSIR-NPL) Campus, Dr. K S Krishnan Marg, New Delhi 110012, India

³Computation and Networking Facility, CSIR-National Physical Laboratory, New Delhi 110012, India

(Received 16 February 2016; accepted 14 May 2016; published online 1 June 2016)

The SrZrO₃ is a well known high-k dielectric constant (~22) and high optical bandgap (~5.8 eV) material and one of the potential candidates for future generation nanoelectronic logic elements (8 nm node technology) beyond silicon. Its dielectric behavior is fairly robust and frequency independent till 470 K; however, it suffers a strong small-polaron based electronic phase transition (T_e) linking 650 to 750 K. The impedance spectroscopy measurements revealed the presence of conducting grains and grain boundaries at elevated temperature which provide energetic mobile charge carriers with activation energy in the range of 0.7 to 1.2 eV supporting the oxygen ions and proton conduction. X-ray photoemission spectroscopy measurements suggest the presence of weak non-stoichiometric O²⁻ anions and hydroxyl species bound to different sites at the surface and bulk. These thermally activated charge carriers at elevated temperature significantly contribute to the polaronic based dielectric anomaly and conductivity. Our dielectric anomaly supports pseudo phase transition due to high degree of change in ZrO₆ octahedral angle in the temperature range of 650–750 K, where electron density and phonon vibration affect the dielectric and conductivity properties. *Published by AIP Publishing.* [<http://dx.doi.org/10.1063/1.4952710>]

I. INTRODUCTION

SrZrO₃ (SZO) is one of the best high-k dielectric, useful for beyond silicon technology memory and logic devices.^{1–8} Extensive studies have been carried out for the three known high temperature phase transitions in SZO, i.e., orthorhombic (*Pnma*) → orthorhombic (*Cmcm*) → tetragonal (*I4/mcm*) → cubic (*Pm3̄m*) at 970 K, 1100 K, and 1440 K, respectively.^{9–11} However, Kennedy and Howard predicted that group theory restricts continuous phase transition from orthorhombic (*Pnma*) at 300 K → orthorhombic (*Cmcm*) at 970 K.¹² The tilted angle of ZrO₆ octahedra leads to several phase transitions as function of temperature and pressure. The tilt angle significantly decreases with increase in temperature which causes several structural phase transitions.^{9–12} At elevated temperature, some situation arises where there is no genuine structural phase transition but the higher degree of reduction in ZrO₆ octahedral angle significantly modifies electron density and phonon vibration. Several techniques have been utilized by researchers to understand the high temperature phase transitions. Ligny and Richet studied the thermal expansion and heat capacity of SZO over large range of temperature and found sharp anomaly near the phase transition temperature.¹³ Kennedy and Howard utilized the high temperature x-ray diffraction (XRD) study to confirm the structural phase transitions.¹² Fujimori *et al.* explained the various high temperature phase transitions of SZO by Raman spectroscopy.¹⁴ To the best of our knowledge, hardly any

work has been carried out in the intermediate temperature range and with the aim to utilization for ionic conductors. Trivalent cations doped SZO systems have been considered for proton-conductors due to the natural presence of hydroxyl group.¹⁵ These systems show increased fast ionic conduction at elevated temperature suitable for hydrogen gas sensors and solid oxide fuel cells (SOFC).

Most of the research activities were focused on the high temperature structural phase transitions. However, other several functional properties and applications for SZO have been reported in the literature. These properties are as follows: dielectric,¹⁶ luminescence,¹⁷ and protonic conductivity on Sc and Y stabilized SZO.¹⁸ The Y/Sc stabilized ZrO₂ is a well known candidate for SOFC and it is being used as an electrolyte in the existing SOFC technology.^{19,20} The impedance spectroscopy technique, which is a well known non-destructive process to characterize the electrical properties, has been extensively utilized to check the suitability of oxide ion conductors for important electrochemical devices such as SOFC, oxygen separation membranes, and sensors.²¹

The present investigation deals with the possible strong polaronic-electronic phase transition between 650 and 800 K. Impedance spectroscopy is an important investigating tool which clearly provides the inside electrical equivalent circuits of microstructures and their contributions to various types of ionic and electronic conductivity. We have categorically applied the dielectric and impedance spectroscopy to understand the bulk and grain boundaries contributions and their active participation for ionic conduction. It would be great if someone tests this system and its ionic conduction as

^{a)}Author to whom correspondence should be addressed. Electronic mail: ashok553@nplindia.org

function of different oxygen and hydrogen partial pressures which is beyond the scope of present investigation. The activation energy calculated from various impedance techniques suggests the possible protonic and oxygen ion conduction at elevated temperature.

II. EXPERIMENTAL DETAILS

The polycrystalline SZO ceramic samples were synthesized by conventional solid state reaction route. The initial ingredients SrCO_3 and ZrO_2 from Sigma Aldrich (purity $\sim 99.9\%$) were mixed in (1:1) stoichiometric ratio and milled homogeneously in pestle-mortar with isopropyl alcohol (IPA) for 2 h. The green powder was dried and calcined at 800°C for 10 h; later, the calcined powder was reground and mixed with a binder (10 wt. % polyvinyl alcohol solution) in order to prepare pellets for sintering. The binder mix granulated powder was shaped into circular disc having diameter 13 mm and thickness 1–1.5 mm under uniaxial pressure of 5–6 tons per square inch. Finally, these pellets were sintered in air at 1400°C for 6 h to achieve 95%–98% of theoretical density. The crystallinity and phase purity of SZO were checked by XRD (Bruker AXS D8 Advance X-ray diffractometer) using the Cu-K_α ($K_\alpha = 1.54059 \text{ \AA}$) monochromatic radiation, in 2θ range between 20° and 80° . Grain growth, surface morphology, and elemental analysis on sintered pellets were carried out using a scanning electron microscope (SEM, Zeiss EVO MA-10) with measuring uncertainty of $\pm 5\%$. Electrical properties of the sintered SZO were measured in metal–insulator–metal (Ag/SZO/Ag) capacitor structures using silver electrode on both sides of pellets. Temperature-dependent dielectric measurements were carried out on Ag/SZO/Ag capacitor at various frequencies (100 Hz to 1 MHz) and temperatures (300–800 K) using LCR meter (HIOKI-3532-50) at an oscillating amplitude of 0.5 V. X-ray photoemission spectroscopy (XPS) measurements were performed by using an Omicron μ -metal ultra-high vacuum (UHV) system equipped with a monochromatic Al K_α X-ray source ($h\nu = 1486.7 \text{ eV}$) and a multi-channeltron hemispherical electron energy analyzer (EA 125). The uncertainty in determining the values of peak positions and full width at half maximum (FWHM) is estimated to be $\pm 0.05 \text{ eV}$.

III. RESULTS AND DISCUSSION

A. Crystal structure and microstructure

Fig. 1 shows the room temperature XRD patterns of the SZO system palletized at 1400°C . XRD data have successfully refined using Rietveld analysis which fitted well for orthorhombic crystal structure with space group $\sim Pnma$ lattice constants $a = 5.7940 \text{ \AA}$, $b = 5.8147 \text{ \AA}$, and $c = 8.1997 \text{ \AA}$, χ^2 : 3.11, Bragg R-factor: 7.33, R_f -factor: 9.66, R_p : 18.5, R_{wp} : 28.9, and R_{exp} : 16.39. Our fitted parameters, crystal structure, and occupancy of elements at various crystallographic positions matched well with the previous reports.^{9–12} Once we established the phase purity and crystal structure of SZO, we investigated the surface topography of pellet to check the distribution of grains, grain boundaries, voids, and porosity. Inset of Fig. 1 indicates homogeneous distribution of grains

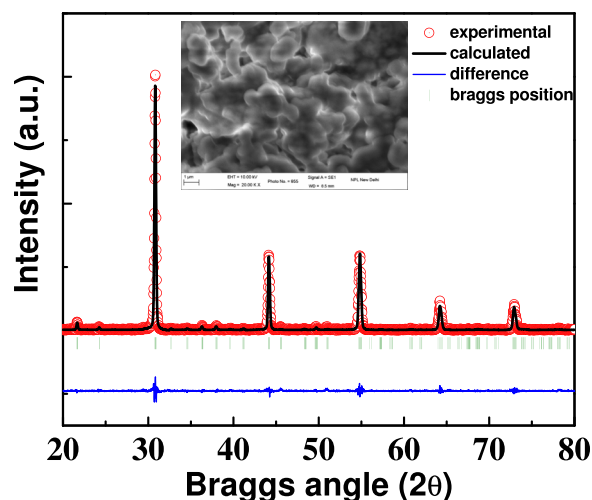


FIG. 1. Experimental x-ray diffraction pattern (red open circles) along with calculated pattern (black thick line) obtained from Rietveld refinement analysis. Blue thin line and green bars represent difference pattern between experimental and calculated diffraction pattern and Bragg positions, respectively. Inset shows the SEM image representing the surface topography of grains and grain boundaries.

in matrix with overlapping grain boundaries. A negligible amount of porosity and voids were observed over the top surface of matrix. It can be also observed from topography image of SZO grains that these grains and grain boundaries appear like hot melted magma which may be due to high temperature fabrication process of ceramics. The elemental analysis gives the molar ratio of SZO nearly 1:1:3 (Sr:Zr:O), respectively, within the experimental limit of energy dispersive x-ray analysis (EDX).

B. Dielectric spectroscopy

Temperature dependent dielectrics spectra show frequency independent dielectric constant with magnitude ~ 22 till 450 K; with further increase in temperature, it started increasing exponentially as shown in Fig. 2. The magnitude of tangent loss over wide range of probe frequency was small ($< 5\%$ at 1 MHz) in the temperature range of 300–450 K which makes SZO a suitable high- k dielectric for logic and memory elements; however, dielectric constant and loss both increase at elevated temperatures. The increase in the magnitude of dielectric constant and its dielectric dispersion above 450 K is mainly due to the thermally activated mobile charge carriers. Fig. 2 shows the high dielectric dispersion, high dielectric loss, and a dielectric maximum in low frequency data in the range of 650–750 K. These dielectric maxima temperatures also shifted with increasing probe frequencies which indicates a strong electron-phonon (small polarons) coupling in these temperature regions.²² In the internal structure of the ZrO_6 , octahedral bond length significantly increases at the bond angles along the $\text{Zr-O}(1)\text{-Zr}$ (156.5°) and $\text{Zr-O}(2)\text{-Zr}$ (156.3°) toward more higher crystal symmetry side (for cubic symmetry, bond angle is around 180°) with increase in temperature, which in turn boosts the presence of small polarons in matrix. The kinks in dielectric spectra represent the pseudo polaronic-electronic phase transition as predicted by Kennedy and Howard,¹² where they

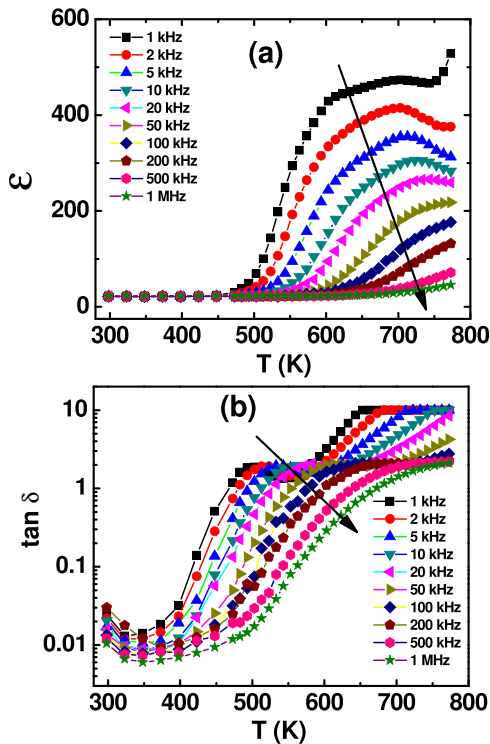


FIG. 2. Dielectric measurements (a) dielectric constant, and (b) tangent loss behavior of SZO over 300–800 K and in the frequency range of 1 kHz to 1 MHz, arrows represent the direction of increasing probe frequency.

suggested that group theory does not permit the direct phase transition from orthorhombic ($Pnma$) at 300 K \rightarrow orthorhombic ($Cmcm$) at 970 K. These dielectric results suggest that there may be subtle pseudo structural phase transition due to the significant tilting of ZrO_6 octahedral and screening among the electrons and the polaronic charge species. We would also like to emphasize that one should not confuse with the similar type of dielectric dispersion in relaxor, where tangent loss shows low loss for low frequency and high for high probe frequencies contrary to the present investigation, where tangent loss is very high for low probe frequency.

C. Impedance spectroscopy

The impedance spectroscopy study has been carried out in high temperature (>550 K) dielectric dispersion region. It indicates two distinct well defined semicircles in the Nyquist plot (Fig. 3) which represents the contribution of grains and grain boundaries in electrical and dielectric properties. The polycrystalline SZO samples are mainly made of grains (bulk) and grain boundaries (connecting area among the grains). Both grains and grain boundaries may contain voids, defects, trap charges, space-charges, etc.; however, it would be hard to distinct the electrical response due to these defects. Grain boundaries area mainly consist electronic polarization since it has no lattice contributions (ionic, dipolar). Electronic polarization, ionic polarization, and dipolar polarization are the main source of contribution to the dielectric and impedance properties of materials in radio frequency regions. The different constituents of dielectric (electronic

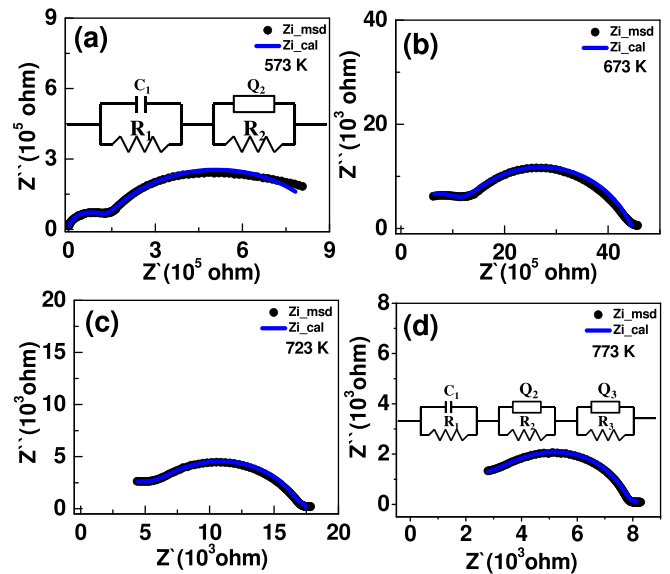


FIG. 3. Nyquist plot of SZO bulk electro-ceramic at (a) 573 K, (b) 673 K, (c) 723 K, and (d) 773 K. Equivalent circuit models of the microstructure behavior are given in Fig. 3(a) for below 673 K and (d) above 700 K.

polarization, ionic polarization, and dipolar polarization) which contribute to the total dielectric polarizability of materials interact with different regions of probe frequencies. The resistance-capacitance (RC) components of electrode-electrolyte, grain boundaries, and grains follow low to high probe frequencies and provide relaxation peaks in dielectric or impedance loss spectra, respectively. It can be seen from Fig. 3 that both bulk and grain boundaries resistance decreased 2–3 orders in magnitude from 573 K to 773 K. The measured impedance data at 573 K and 673 K were fitted with the equivalent circuit given in the inset of Fig. 3(a). The values of the coefficients (n) of grains and grain boundaries constant phase element (CPE) in the range of 0.72–0.80 ($Z_{CPE} = 1/Y_{CPE} = (1/Q_0\omega^n) * e^{-\pi ni/2}$, where $0 \leq n \leq 1$) suggest that both grains and grain boundaries are arranged in brick-layer model with series connection. At high temperature, a small resistive element was also observed in low frequency region that represents the electrode-electrolyte contribution. The impedance behavior is similar to the oxygen/protonic ion conduction in rare earth stabilized zirconia.²³ The impedance data at 723 K and 773 K were fitted with the equivalent circuit given in the inset of Fig. 3(d). It indicates that grains and grain boundaries are highly conducting in nature and the mobile charge carriers responsible for conduction process have moderate or low activation energy $E_g \sim 0.67$ eV for grains and E_{gb} 0.83 to 1.2 eV for grain boundaries.²⁴ These activation energies are ideal for oxygen ions or proton conduction. The resistance of bulk as well as grain boundaries decreases almost 3–4 orders in magnitude (from M Ω to few k Ω). Fig. 4 shows impedance loss spectra as function of frequency in which relaxation frequency shifted towards higher frequency side with increase in temperature. Two distinct impedance loss peaks were observed: low frequency peak was associated with grain boundaries, whereas high frequency peak represents relaxation behavior of charge carriers associated with bulk. Since

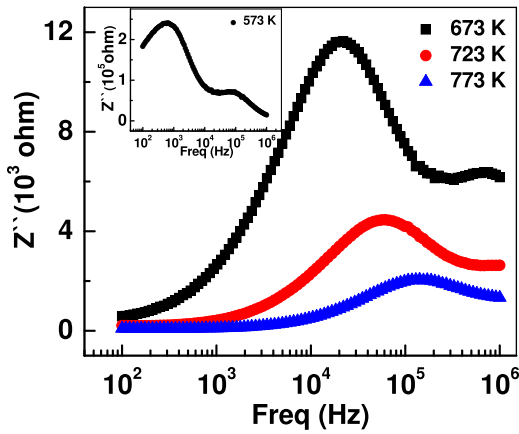


FIG. 4. Impedance loss spectra as function of frequency and temperature, inset shows two clear impedance loss peaks due to grains and grain boundaries which shifted to higher frequency side with increase in temperature.

grains have more lattice (electronic, ionic, and dipolar) contribution, their RC components follow higher probe frequency compared to the grain boundaries (mainly electronic). The relaxation (RC circuit) peaks of respective dielectric/impedance loss spectra shifted to higher frequency side with increasing temperature or energy of charge carriers. It indicates that the relaxation time (inverse of relaxation frequency) of charge carriers associated with bulk and grain boundaries decreases monotonically with increase in temperature as charge carriers hop among the nearest neighbor sites very fast (small time). These charge carriers obey the following relation: $\omega_{\max}\tau = 1$, where ω_{\max} is the peak relaxation frequency and τ is the relaxation time. The activation energies of bulk and grain boundaries were calculated using the equation $\tau = \tau_0 e^{-\frac{E_a}{k_B T}}$, where τ is the relaxation time, τ_0 is the time constant, k_B is Boltzmann constant, T is the temperature, and E_a is the activation energy. The activation energies obtained by different processes are in the range of 0.67 to 1.2 eV as shown in Fig. 5 with detail in figure caption. The Arrhenius plot of ac conductivity as function of inverse temperature for various frequencies provides the E_a in the same range. The E_a decreases with increase in probe frequency (Fig. 5(b)); however, this energy is good enough to transport the oxygen vacancies and protons across the electrode. The oxygen vacancies and hydroxyl cations in the stoichiometric SZO composition naturally developed during the high temperature sample processing. The evidence of the presence of hydroxyl ions and oxygen vacancies has been found in XPS study, and it will be discussed in detail in Section III E. In any oxide, one cannot rule out the intrinsic electronic contribution in transport properties; however, keeping in mind that SZO has very high bandgap ($E_g \sim 5.4$ eV) and the observed $2E_a < E_g$, it is unlikely to be very large contribution from the electronic charge carriers. In general, the electron mobility is several orders higher than the ionic mobility; hence, small amount of electronic charge carriers significantly affect the overall electrical conductivity.²⁴ However, the kinetic of the oxygen exchange reaction becomes more significant at elevated temperature >700 K. An equilibrium condition may establish between the oxygen gas phase and oxygen in lattice following the defect oxidation condition given by

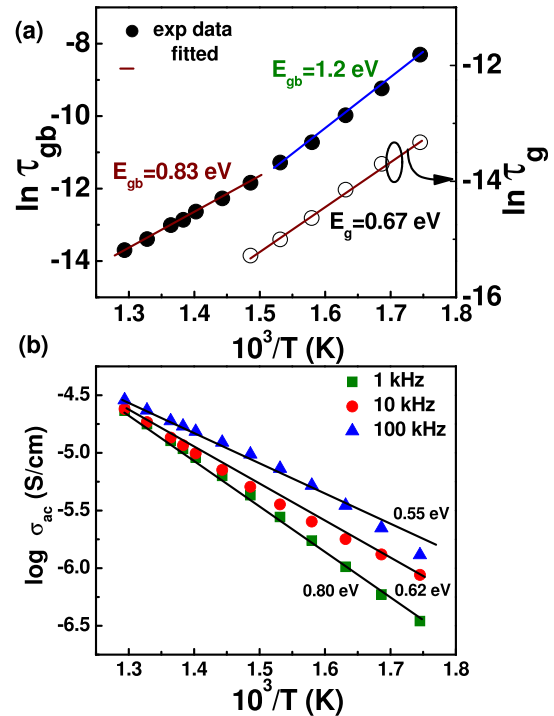


FIG. 5. (a) Shows the liner fit of the relaxation time and related activation energy for grains (left) and grain boundaries (right), (b) ac conductivity as function of inverse temperature and obtained activation energy for various probe frequencies.

$\frac{1}{2}O_2(g) + V_o'' \rightleftharpoons O_o^\times + 2h'$, where $O_2(g)$ is the oxygen in gas phase, V_o'' is the oxygen vacancies, O_o^\times is the oxygen in lattice, and h' is the free holes. As we have also observed naturally occurring hydroxyl ion in SZO matrix which plays an important role in the conduction process and it implied that oxygen vacancies react not only with oxygen but also with water vapor and vice versa, $H_2O(g) + O_o^\times + V_o'' \rightleftharpoons 2OH_o'$, where $H_2O(g)$ is the water vapor and OH_o' is the hydroxyl ions. The main ionic conductivity measurement processes are as follows: (i) use of proper ion-conducting electrode but electron-blocking electrode or measure the ionic transference number, (ii) four point measurement geometries in dc mode, and (iii) frequency-dependent impedance spectroscopy studies. We have used the last method and explained the behavior of mobile charge carriers.²⁴

D. ac conductivity

The ac conductivity of SZO as function of frequency is shown in Fig. 6. The ac conductivity plots of SZO show the following characteristics: (i) almost frequency dependent conductivity below 450 K, (ii) in the temperature range of 450 K to 550 K, ac conductivity shows small dc plateau in low frequency region with a strong frequency dependent conductivity window for high frequency region, (iii) above 550 K, frequency independent conductivity in low frequency regions (<1 kHz), a frequency dependent conductivity in mid and high frequency regions, (iv) above 700 K, almost frequency independent conductivity below 50 KHz frequency, and (v) an enhancement of 4–5 order of dc conductivity with increase in temperature (from 300 K to 773 K).

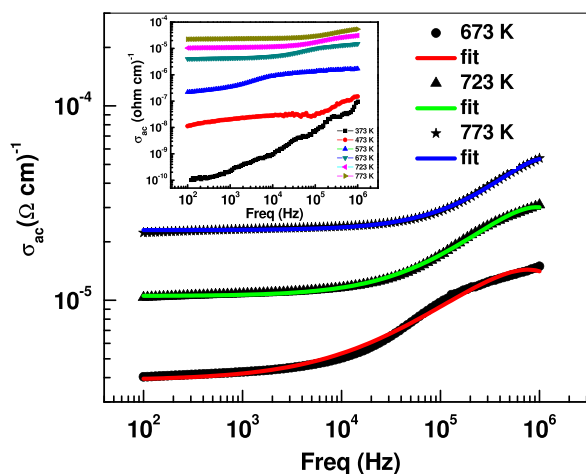


FIG. 6. Plot of ac conductivity as function of frequency at various temperatures and their fitting with double power laws, inset shows frequency dependent ac conductivity from 300 K to 773 K.

The above mentioned observations in conductivity spectra can be explained on the basis of jump relaxation model and conduction through grains and grain boundaries. The higher temperature (>650 K) and low frequency dc conductivity (σ_{DC}) is attributed due to long-range translational motion of charge carriers. The observed frequency independent dc conductivity (higher temperature) was explained by Funke in the jump relaxation model (JRM).^{25–27} JRM suggests that the thermally active mobile charge carriers successfully hop in the nearest neighbor site due to long relaxation time. However, in present case, the relaxation time monotonically increases with increase in temperature for low frequency. Above 650 K, two competing relaxation

processes take place in mid frequency region (>1 kHz and <100 kHz), where (i) charge carriers sometime unsuccessfully hop to its initial position and (ii) in some cases, the charge carriers successfully hop to new sites due to fast relaxation process. Fig. 6 shows the modified Jonscher double power law fitting of the experimental data using the equation mentioned below^{25–27}

$$\sigma(\omega) = \sigma(0) + A_1\omega^{n_1} + A_2\omega^{n_2}, \quad (1)$$

where $\sigma(\omega)$ is the total conductivity, the first term $\sigma(0)$ is the frequency independent conductivity which corresponds to the translation long-range charge carriers motion. The second term $A_1\omega^{n_1}$ represents the region II, the exponent $0 < n_1 < 1$ characterizes the competing translational hopping motion (back and forth short range hopping). The third term $A_2\omega^{n_2}$ illustrates localized or reorientational hopping motion with exponent $1 < n_2 < 2$.²³ The values for n_1 and n_2 in the temperature range from 650 to 773 K were found to vary between 0.8–0.95 and 1.1–1.8, respectively. The values of both exponents increase with increasing temperature support concept of small polaron hopping mechanism.²²

E. X-ray photoemission spectroscopy

The survey, O 1s, Sr 3d, and Zr 3d spectra of SZO sample sintered at 1400°C are displayed in Figs. 7(a)–7(d), respectively. Fig. 7(a) shows the survey spectrum of the sample over wide binding energy (BE) and all the features are related to constituent elements of SZO. No features related to any impurity were found in the spectrum except small carbon trace at 285.0 eV (C 1s) which may be due to high sintering temperature of the sample. The spectrum is taken after

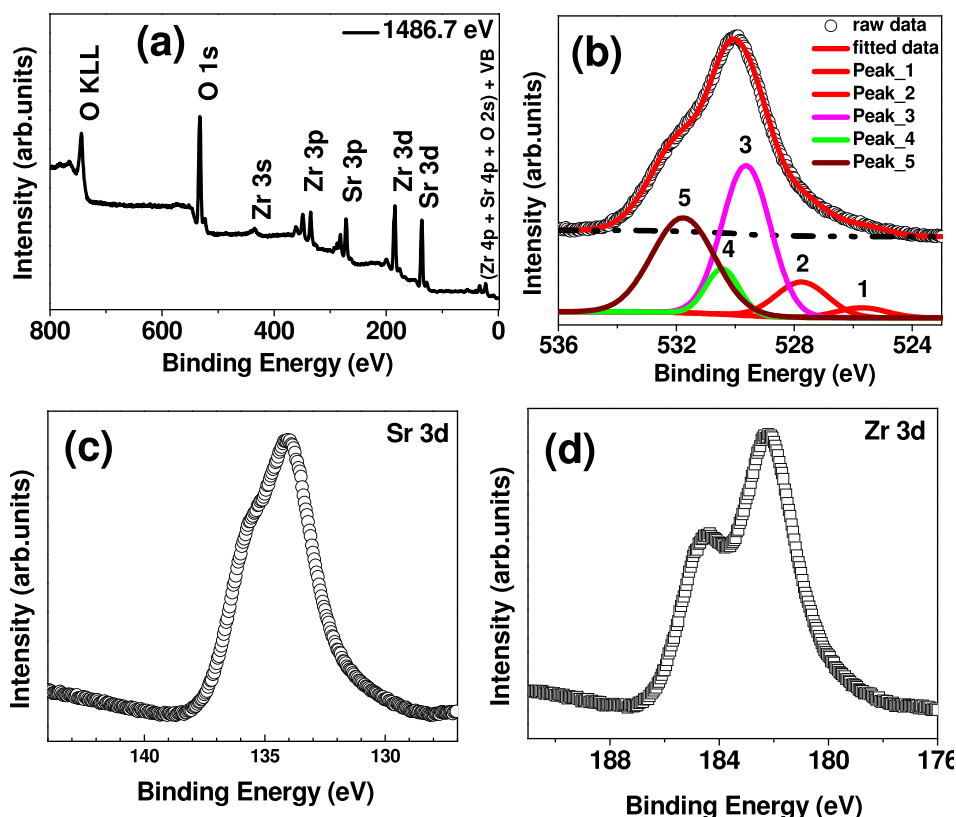


FIG. 7. (a)–(d) XPS measurements demonstrate the XPS data of SZO, (a) survey spectrum for elemental presence, (b) O 1s core level spectrum along with fitting components for various types of oxygen elements, (c) Sr 3d, and (d) Zr 3d core levels.

in-situ heat treatment at 250 °C. We have carefully fitted the entire O 1s region with five components corresponding to the five different peaks contributing to this region as shown in Fig. 7(c). The peak positions and full width at half maximum (FWHM) of the five peaks suggest very weak peak 1 and peak 2 at 525.7 eV and 527.8 eV are O²⁻ from non-stoichiometric ZrO_x and O²⁻ from non-stoichiometric SrO_x, respectively. The peak 3 at 529.6 eV is originating from lattice oxygen from the stoichiometric SrZrO₃.

The peaks 4 (530.3 eV) and 5 (531.7 eV) can be attributed to hydroxyl species bound to different sites at the surface and bulk, respectively. The presence of high amount of intrinsic hydroxyl ions is evident since the sample was annealed at 1400 °C and *in situ* annealing treatment at 250 °C was carried out before XPS measurement. The fitted area of the hydroxyl groups bound to different sites at bulk and surface is almost same to that of the area of lattice oxygen from the SZO which in turn provides very high ionic conduction at elevated temperature. The high conductivity with very high activation energy (~1.2 eV) above 750 K supports the possible application of SZO in proton conductors and medium range solid oxide fuel cells (SOFC).

The Sr 3d spectrum exhibits 3d_{5/2} and 3d_{3/2} spin-orbit doublet peaks located at ~134.0 and 135.6 eV, respectively, as shown in Fig. 7(c). The spin-orbit splitting of Sr 3d line is about 1.7 eV in perfect cubic symmetry of SrTiO₃ crystal.²⁸ The spin-orbit splitting value 1.6 eV suggests small octahedral distortion from perfect cubic crystal symmetry. The Zr 3d core level shows 3d_{5/2} and 3d_{3/2} spin-orbit doublet peaks located at ~182.2 and 184.5 eV, respectively, displayed in Fig. 7(d). The spin-orbit splitting of Zr 3d is found to be around 2.3 eV. The peaks around 530.3 eV and 531.7 eV due to hydroxyl species are at slightly higher BE side compared to the earlier report which suggests that the magnitude of naturally occurring charge species was caused in the small shift of Fermi level position towards conduction band side resulting in more favorable situation for ionic conduction.¹⁸

IV. CONCLUSIONS

A careful dielectric, impedance, and conductivity spectroscopy has been carried out on SZO over wide range of temperature and frequency that suggests small polaron based pseudo phase transition in the range of 650 to 750 K. Bulk as well as grain boundaries play important role in high temperature conduction process. Nyquist plot and impedance loss spectra suggest that bulk and grain boundaries become conducting above 600 K and the magnitude of resistance decreased 4–5 orders compared to room temperature resistance. The activation energies obtained from various methods in the range of 0.7 to 1.2 eV support the oxygen ion and proton conduction. XPS study suggests the existence of intrinsic hydroxyl ions and ZrO₆ octahedral distortion from perfect cubic structure. The ac conductivity data follow JRM model

with various competing translational and reorientational hopping of charge carriers, and their frequency exponents indicate small polaron supported conductivity.

ACKNOWLEDGMENTS

A.K. acknowledges the CSIR-MIST (PSC-0111) project for the financial assistance. Hitesh Borkar would like to acknowledge the UGC (SRF) to provide fellowship to carry out Ph. D program. Authors would like to thank Dr. V. N. Ojha (Head ALSIM), Dr. Sanjay Yadav, and Dr. H. K. Singh for their constant encouragement and support.

- ¹G. E. Moore, *Electron. Mag.* **38**, 8 (1965).
- ²X. B. Lu, G. H. Shi, J. F. Webb, and Z. G. Liu, *Appl. Phys. A* **77**, 481–484 (2003).
- ³A. I. Kingon, J.-P. Maria, and S. K. Streiffer, *Nature* **406**, 1032 (2000).
- ⁴S. P. Pavunny, R. Thomas, A. Kumar, E. Fachini, and R. S. Katiyar, *J. Appl. Phys.* **111**, 044106 (2012).
- ⁵G. D. Wilk, R. M. Wallace, and J. M. Anthony, *J. Appl. Phys.* **89**, 5243 (2001).
- ⁶L. Weston, A. Janotti, X. Y. Cui, C. Stampfl, and C. G. Van de Walle, *Phys. Rev. B* **89**, 184109 (2014).
- ⁷T. Yajima, H. Suzuki, T. Yogo, and H. Iwahara, *Solid State Ionics* **51**, 101 (1992).
- ⁸M. K. Singh, G. Singh, T. H. Kim, S. Kojima, R. S. Katiyar, and J. F. Scott, *EPL* **107**, 26004 (2014).
- ⁹L. Carlsson, *Acta Crystallogr.* **23**, 901 (1967).
- ¹⁰A. Ahtee, M. Ahtee, A. M. Glazer, and A. W. Hewat, *Acta Crystallogr. B* **32**, 3243 (1976).
- ¹¹A. Ahtee, A. M. Glazer, and A. W. Hewat, *Acta Crystallogr. B* **34**, 752 (1978).
- ¹²B. J. Kennedy, C. J. Howard, and B. C. Chakoumakos, *Phys. Rev. B* **59**, 4023 (1999).
- ¹³D. DeLigny and P. Richet, *Phys. Rev. B* **53**, 3013 (1996).
- ¹⁴H. Fujimori, M. Kakihana, K. Ioku, S. Goto, and M. Yoshimura, *J. Ceram. Soc. Jpn.* **112**, 189–192 (2004).
- ¹⁵T. Higuchi, T. Tsukamoto, N. Sata, K. Hiramoto, M. Ishigame, and S. Shin, *Jpn. J. Appl. Phys., Part 1* **40**, 4162 (2001).
- ¹⁶R. V. Shende, D. S. Krueger, G. A. Rossetti, Jr., and S. J. Lombardo, *J. Am. Ceram. Soc.* **84**, 1648 (2001).
- ¹⁷V. M. Longo, L. S. Cavalcante, A. T. de Figueiredo, L. P. S. Santos, E. Longo, J. A. Varela, J. R. Sambrano, C. A. Paskocimas, F. S. De Vicente, and A. C. Hernandez, *Appl. Phys. Lett.* **90**, 091906 (2007).
- ¹⁸T. Higuchi, T. Tsukamoto, H. Matsumoto, T. Shimura, K. Yashiro, T. Kawada, J. Mizusaki, S. Shin, and T. Hattori, *Solid State Ionics* **176**, 2435 (2005).
- ¹⁹A. Kumar and I. Manna, *Physica B: Condens. Matter* **403**(13), 2298–2305 (2008).
- ²⁰B. C. H. Steele and A. Heinzl, *Nature* **414**, 345–352 (2001).
- ²¹M. L. Marthia, J. Pietrowski, R. A. De Souza, H. Zhang, I. M. Reaney, S. N. Cook, J. A. Kilner, and D. C. Sinclair, *Nat. Mater.* **13**, 31–35 (2014).
- ²²L. Weston, A. Janotti, X. Y. Cui, B. Himmetoglu, C. Stampfl, and C. G. Van de Walle, *Phys. Rev. B* **92**, 085201 (2015).
- ²³D. Pergolesi, E. Fabbri, A. D. Epifanio, E. D. Bartolomeo, A. Tebano, S. Sanna, S. Licocchia, G. Balestrino, and E. Traversa, *Nat. Mater.* **9**, 846–852 (2010).
- ²⁴R. A. De Souza, *Adv. Funct. Mater.* **25**, 6326–6342 (2015).
- ²⁵A. K. Jonscher, *Nature* **267**, 673 (1977).
- ²⁶K. Funke, *Prog. Solid State Chem.* **22**, 111 (1993).
- ²⁷A. P. Almond, A. R. West, and R. J. Grant, *Solid State Commun.* **44**, 1277 (1982).
- ²⁸P. Pal, P. Kumar, V. Aswin, A. Dogra, and A. G. Joshi, *J. Appl. Phys.* **116**, 053704 (2014).